

Understanding Heart Failure Through Multi-Scale Modeling

Brianna Chrisman, Advisor Stuart Campbell

2015 Senior Thesis for Yale University, Department of Biomedical Engineering

Abstract. Heart failure is a contributing cause in one in nine American deaths, and over half of patients diagnosed with heart failure die within five years of diagnosis. A number of factors have been shown to correlate with a risk for heart failure, but the complex nature of the cardiac cycle on both a cellular and systems level make deeply understanding the mechanics of heart failure difficult. We present a multi-scale model combining electrophysiology, myofilament, left ventricular, and circulatory system models. We explore the effects of small-scale and system-level changes on cardiac performance and show that our model can accurately predict heart failure when a number of different deficiencies are introduced.

1 Introduction and Background

Heart failure, the inability of the heart to sufficiently pump blood to the rest of the body is a profound health problem in America. Heart failure is a contributing cause to one in nine American deaths, and there is a 50% five-year mortality rate for those diagnosed with heart failure [1]. While a number of environmental and genetic factors, such as alcohol abuse, diabetes, and congenital heart defects are known to increase the risk of heart disease, the complex nature of the heart has limited our ability to obtain a deep understanding of the mechanics behind heart failure [2].

Animal experiments have limited capacity in helping us understand heart failure. In addition to being expensive and time-consuming, many experiments require collecting data that is extremely hard to gather. For example, only in 2012 did a group develop an effective method for measuring arterial strain without causing vessel constriction and affecting the measurements [3].

Furthermore, even if animal experiments were feasible to run on a large-scale, the human heart has a number of behaviors different than those in animal hearts. For example, canines, whose hearts are comprised of the same heart chambers and valves as the heart, have significantly faster heartbeats than humans, have much more irregular heartbeats, and do not suffer heart attacks like humans because they have no fatty buildup in their blood vessels [4].

Computational modeling has emerged as a valuable tool in studying cardiac performance. After Alan Lloyd Hodgkin and Andrew Huxley developed their famous model for action potential in the 1960s, Di Francesco Noble extended the Hodgkin-Huxley model to describe the cardiac action potential in Purkinje cells [5]. The cross-bridge cycle of muscle contraction has been modeled in a number of different ways: as a Monte Carlo simulation [6] and as a multi-state Markov process as in [7], to name some. Computational models of blood flow have existed for a number of decades, and rely on lumped parameter models based on electrical circuit components [8]. Multi-scale modeling, computational modeling over different biological scales of time and space, has arisen as a particularly viable tool for understanding the emergent properties of the different scales in which we can study the cardiac cycle.

The cardiac cycle is the process by which the heart pumps blood to the rest of the body. It is composed of two main stages. One is systole, during which a stimulus from the sinoatrial node pacemaker cell causes the cardiac muscle cells (cardiomyocytes) to contract, building up pressure within the left ventricle and ejecting blood from the left ventricle to the rest of the body. The second stage is diastole, during which the ventricles fill and relax. This delicate cycle requires cooperation of a number of physiological processes: voltage-gated ion channels respond to the pacemaker stimulus and produce a cardiac action potential and corresponding calcium transient. This increase in intracellular calcium allows the cross-bridge cycle to take place, during which

actin and myosin alternately bind and unbind to cause the “powerstroke” that is characteristic of muscle contraction. And finally, valves within the heart open and close in order to allow discrete stages of ejection, isovolumetric relaxation, filling, and isovolumetric contraction [9].

We present a multi-scale model that integrates the cellular and system levels of the cardiac cycle, allowing us to understand how micro-scale changes affect cardiac performance on a large scale.

2 Methods

In order to understand how small scale protein and cellular level changes affect the cardiac system macroscopically, we needed to create a model that spanned a number of biological scales. Our final model uses four sub-models, each encompassing different scales. The electrophysiology model describes the activity of ion gates on the membrane and sarcoplasmic reticulum of a single cardiac cell. The myofilament model describes the mechanics of the troponin-tropomyosin-actin-myosin protein complex and the cooperation of neighboring complexes to produce force within the tissue. The left ventricle model describes the geometry of the heart and the translation of sarcomere force and length into pressure and volume. The circulatory system model couples the heart with the systemic blood vessels to obtain a closed-loop description of systemic blood flow.

2.1 *Electrophysiology Model*

We modeled the electrophysiological response of the myocyte to a cardiac pacemaker stimulus using the ten-Tusscher model for ventricular tissue [10]. The ten-Tusscher model describes the activity of 12 transmembrane currents: fast Na^+ (I_{Na}), L-type Ca^{2+} (I_{CaL}), delayed rectifier K^+ rapid (I_{Kr}) and slow (I_{Ks}), inward rectifier K^+ (I_{K1}), transient outward K^+ (I_{to}), plateau

K^+ (I_{pK}), Na^+ - Ca^{2+} exchanger (I_{NaCa}), Na^+ - K^+ pump (I_{NaK}), sarcolemmal Ca^{2+} pump (I_{pCa}), and background Na^+ (I_{bNa}) and Ca^{2+} (I_{bCa}) currents. We opted for the ten-Tusscher model because it is based entirely off of human data in comparison to models such as Priebe-Beuckelman [11], which rely heavily on animal measurements. Furthermore, ten-Tusscher uses relatively few parameters in comparison with more sophisticated models such as the 67-variable Iyer-Mazhari model [12], making ten-Tusscher a computationally feasible model to use in multi-scale simulations such as ours. The ten-Tusscher model has 17 state variables: 12 gating variables (m , h , j , d , f , f_{Ca} , r , s , x_s , x_{r1} , x_{r2} , g) describing the mechanics of the gates controlling the transmembrane currents, voltage (V), intracellular Na^+ (Na_i) and K^+ (K_i) concentrations, and cytosolic (Ca_i) and sarcoplasmic Ca^{2+} (Ca_{SR}) concentrations.

Equations 1-19 illustrate the central equations governing the voltage, the ion concentrations, and the different currents. Note that in equations 18-19 we have analytically differentiated the equations describing Ca^{2+}_i buffering by calmodin and Ca^{2+}_{SR} buffering by calsequestrin in the original set of equations [10]. We thus obtained the time rate of change for free cytosolic and sarcolemmal Ca^{2+} , rather than total cytosolic and sarcolemmal Ca^{2+} . Table 1 gives the description and typical values for a number of rates. Equations describing variables referenced in the equations and other constants and their values can be found in [10]. Hodgkin-Huxley-type equations describing the states of the gating variables are described in detail in [5].

Voltage:

$$\frac{dV}{dt} = - \frac{I_{stim} + \sum_{channel} I_{channel}}{C_m} \quad (1)$$

Fast Na⁺:

$$I_{Na} = G_{Na} m^3 h j (V - E_{Na}) \quad (2)$$

Transient Outward K⁺:

$$I_{to} = G_{to} r_s (V - E_K) \quad (3)$$

Slow Rectifier K⁺:

$$I_{Ks} = G_{Ks} x_s^2 (V - E_{Ks}) \quad (4)$$

Rapid Rectifier K⁺:

$$I_{Kr} = G_{Kr} \sqrt{\frac{K_o}{5.4}} x_{r1} x_{r2} (V - E_K) \quad (5)$$

Inward Rectifier K⁺:

$$I_{Kl} = G_{Kl} \sqrt{\frac{K_o}{5.4}} x_{Kl\infty} (V - E_K) \quad (6)$$

Na⁺-Ca²⁺ Exchanger:

$$I_{NaCa} = \frac{k_{NaCa} \exp(\gamma F / RT) Na_i^3 Ca_o - \exp((\gamma - 1) VF / RT) Na_o^3 Ca_o \alpha}{(K_{mNa}^3 + Na_o^3)(K_{mCa} + Ca_o)(1 + k_{sat} \exp((\gamma - 1) VF / RT))} \quad (8)$$

Sarcoplasmic leakage Ca²⁺:

$$I_{leak} = V_{leak} (Ca_{SR} - Ca_i) \quad (10)$$

Na⁺-K⁺ Pump:

$$I_{NaK} = P_{NaK} \frac{K_o Na_i}{(K_o + K_{mK})(Na_i + K_{mNa})(1 + .1245 \exp(-.1 VF / RT) + .0353 \exp(-VF / RT))} \quad (12)$$

Plateau K⁺:

$$I_{pK} = G_{pK} \frac{V - E_K}{1 + \exp((25 - V) / 5.98)} \quad (13)$$

Intracellular Na⁺:

$$\frac{dNa_i}{dt} = - \frac{I_{Na} + I_{bNa} + 3I_{NaK} + 3I_{NaCa}}{V_c F} \quad (16)$$

Sarcoplasmic Ca²⁺:

$$\frac{dCa_{SR}}{dt} = \frac{V_c (-I_{leak} + I_{up} - I_{rel})}{V_{SR} \frac{Buf_{SR} K_{bufSR}}{(K_{bufSR} + Ca_{bufSR})^2}} \quad (18)$$

Table 1: Ten-Tusscher Variables and Parameters

Var.	Description	Units
E _x	Electrochemical potential of ion x	mV
G _y	Maximal conductance of channel y	nS/pF
F	Faraday constant	C/mmol
R	Gas Constant	J K ⁻¹ mol ⁻¹
T	Temperature	K
x _o	Extracellular concentration of ion x	μM
x _i	Intracellular concentration of ion x	μM
K _y	Half-saturation constant for channel y	μM
I _y	Current though channel	pA/pF
v _c	Cytosolic Volume	μm ³
v _{SR}	Sarcoplasmic reticulum Volume	μm ³
Buf _c	Cytoplasmic buffer concentration	μM
Buf _{SR}	Sarcoplasmic buffer concentration	μM
C _m	Cell capacitance per area	μF/cm ²
V _y	Maximum y current	μM/ms

L-type Ca²⁺:

$$I_{CaL} = G_{CaL} df_{Ca} 4 \frac{VF^2}{RT} \frac{Ca_i \exp(2V / RT) - .341 Ca_o}{\exp(2V / RT) - 1} \quad (7)$$

Sarcoplasmic Ca²⁺ Pump:

$$I_{pCa} = G_{pCa} \frac{Ca_i}{K_{pCa} + Ca_i} \quad (9)$$

Saroplasmic Uptake Ca²⁺:

$$I_{up} = \frac{V_{maxup}}{1 + K_{up}^2 / Ca_i^2} \quad (11)$$

Sarcoplasmic Ca²⁺ Release:

$$I_{rel} = \left(a_{rel} \frac{Ca_{SR}^2}{b_{rel}^2 + Ca_{SR}^2} + c_{rel} \right) dg \quad (11)$$

Background Ca²⁺:

$$I_{bCa} = G_{bCa} (V - E_{Ca}) \quad (14)$$

Background Na⁺:

$$I_{bNa} = G_{bNa} (V - E_{Na}) \quad (15)$$

Intracellular K⁺:

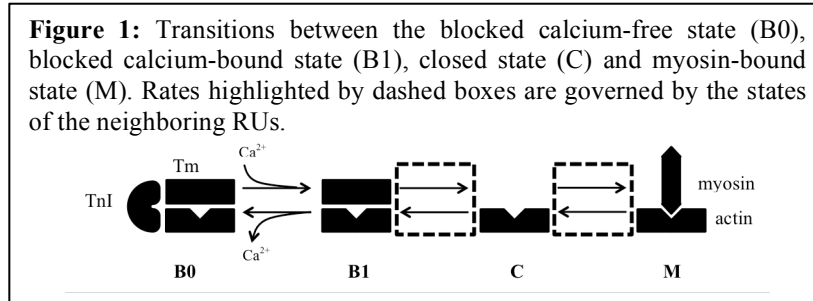
$$\frac{dK_i}{dt} = - \frac{I_{Kl} + I_{to} + I_{Kr} + I_{Ks} - 2I_{NaK} + I_{pK} + I_{stim}}{V_c F} \quad (17)$$

Intracellular Ca²⁺:

$$\frac{dCa_i}{dt} = \frac{\frac{I_{CaL} + I_{CaL} + I_{CaL} - 2I_{CaL}}{2V_c F} + I_{leak} - I_{up} + I_{rel}}{\frac{Buf_c K_{bufc}}{(K_{bufc} + Ca_i)^2}} \quad (19)$$

2.2 Myofilament Model

To describe the states of the cross-bridges and the subsequent force produced by the ventricular tissue in relation to the intracellular calcium concentration, we use a model described by *Campbell et al.* [7]. Some variables and constants are described in Table 2, and the rest can be found in detail in [7]. This model describes a single tropomyosin-actin complex using a four-state system as shown in Figure 1. In the blocked calcium-free states (B0), troponin C is bound to the actin-tropomyosin complex, preventing tropomyosin from sliding and revealing myosin-binding sites on actin. In the blocked calcium-heavy state (B1), calcium binds to troponin I, changing its conformation and causing troponin C to unbind from the actin-tropomyosin complex and to troponin I. Once troponin C is no longer bound to the actin-tropomyosin complex, tropomyosin-sliding can occur allowing actin to reveal its myosin-binding site in the closed state (C). From here, myosin can bind and muscle contraction can occur (M). Rate constants governing transitions between B1 and C and C and M are dependent on the states of neighboring regulatory units.



Muscle contraction, or the powerstroke, was described using a two-state system where the actin and myosin are either in a pre-stroke (M_{pr}) or post-stroke state (M_{po}) with rate changes computed by Eqs. 22-23. We described sarcomere force using both an active and passive component. The passive force was described using an exponential spring-like function in Eq. 24. Active force (Eq. 25) was dependent on the state of the cross-bridge cycle (pre- or post-powerstroke) at any given time as well as sarcomere length. This dependence operated on a force-

sarcomere length curve (the overlap, or O[SL]) that is roughly linear in the regions cardiac contraction operates on.

State transitions:

$$\frac{d}{dt} \begin{bmatrix} B0 \\ B1 \\ C \\ M_{pr} \\ M_{po} \end{bmatrix} = A \begin{bmatrix} B0 \\ B1 \\ C \\ M_{pr} \\ M_{po} \end{bmatrix} \quad (20)$$

Intracellular Calcium:

$$\frac{dCa_i}{dt} = Tn_C(k_u B1 - k_b Ca_i B0) \quad (21)$$

Pre-powerstroke distortion:

$$\frac{dX_{Mpr}}{dt} = - \left(f \frac{C}{M_{pr}} + h_b \frac{M_{po}}{M_{pr}} \right) M_{pr} + \frac{1}{2} \frac{dSL}{dt} \quad (22)$$

Post-powerstroke distortion:

$$\frac{dX_{Mpo}}{dt} = -h_f \frac{M_{po}}{M_{pr}} (X_{Mpo} - X_{Mpo0}) + \frac{1}{2} \frac{dSL}{dt} \quad (23)$$

Passive Force:

$$F_p = \begin{cases} k_p e^{\tau_p (SL - SL_{slack})} & SL > SL_{slack} \\ -k_p e^{\tau_p (SL_{slack} - SL)} & SL \leq SL_{slack} \end{cases} \quad (24)$$

Active Force:

$$F_a = k_{xb} O[SL] (X_{Mpo} M_{po} + X_{Mpr} M_{pr}) \quad (25)$$

Table 2: Myofilament model variables and parameters

Var.	Description
M_{pr}	Percentage of cross-bridges in pre-stroke state
M_{po}	Percentage of cross-bridges in post-stroke state
X_{Mpr}	Pre-stroke distortion factor
X_{Mpo}	Post-stroke distortion factor
SL	Sarcomere length (μm)
SL_{slack}	Sarcomere length with no passive force (μm)
O	Sarcomere overlap active force scaling factor
k_{xb}	Active force scaling factor (μN)
k_p	Passive force scaling factor (μN)
τ_p	Passive force scaling factor ($1/\mu m$)
Tn_C	Intracellular Troponin C concentration (μM)
$B0$	Percentage of RUs in blocked calcium-free state
$B1$	Percentage of RUs in blocked calcium-bound
C	Percentage of RUs in closed state
M	Percentage of RUs in myosin-bound state
A	Matrix of transition rates
f	C-to-M transition rate constant
h_b	Post-to-pre powerstroke rate constant
h_f	Pre-to-post-powerstroke rate constant
k_u	Rate of Ca^{2+} unbinding from TnC
k_b	Binding rate between Ca^{2+} and TnC (μM^{-1})
Ca_i	Intracellular calcium concentration (μM)

Total Force:

$$F_{tot} = F_a + F_p \quad (26)$$

2.3 Left Ventricle

In order to translate between force produced by the sarcomeres and sarcomere length, we approximated the left ventricle as a half-sphere. Using this simplification, we described the relationships between length, force, volume, and pressure using the following geometric equations (Eqs.27-28). Here, V_w is the volume of the ventricular wall, α_{L2V} is a scaling factor between the sarcomere length and the circumference of the left ventricle, and α_{F2P} . To find values

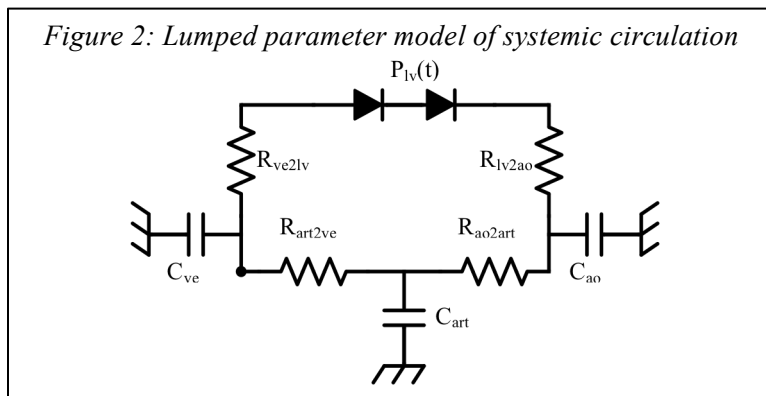
for V_w and the α 's, we fit Eqs. 27-28 to experimental data on systolic and diastolic volumes, pressures, sarcomere forces, and sarcomere lengths. While there is little human data about the values of the scaling factors and V_w , our fitted value for V_w (~ 250 mL) was larger but on the same scale as that measured in a canine hearts (~ 100 mL) [13]. This is what is to be expected since humans are larger than canines and have similar shaped hearts.

$$L = \frac{1}{\alpha_{L2V}} \left(6\pi^2 \left(V(t) + \frac{V_w}{2} \right) \right)^{1/3} \quad (27)$$

$$P = \alpha_{F2P} \left(\left(\frac{V_w}{V} + 1 \right)^{2/3} - 1 \right) F \quad (28)$$

2.4 Circulatory System

We described the circulatory model using a lumped parameter model (Fig. 2), simplified from *Youn et al.* [14] to include only aortic (ao), systemic arterial (art), and systemic venous (ve) compartments. Resistances correspond to vessel resistances to fluid flow, and capacitors to the compliances of the different vessel compartments. Left ventricular pressure (lv) is calculated using the aforementioned sub-models, and the pressures and volumes of each compartmental as well as ventricular volume are governed by Eqs. 29 – 31. We used the values given by [14] for resistances and capacitances. The diodes represent the AV valve and the aortic valve, preventing backflow into the veins when the ventricular pressure is higher than the venous pressure and backflow into the ventricle when the aortic pressure is higher than the ventricular pressure.



Inflow:

$$Q_{in} = \frac{P_j - P_i}{R_{j2i}} \quad (29)$$

Outflow:

$$Q_{out} = \frac{P_i - P_j}{R_{i2j}} \quad (30)$$

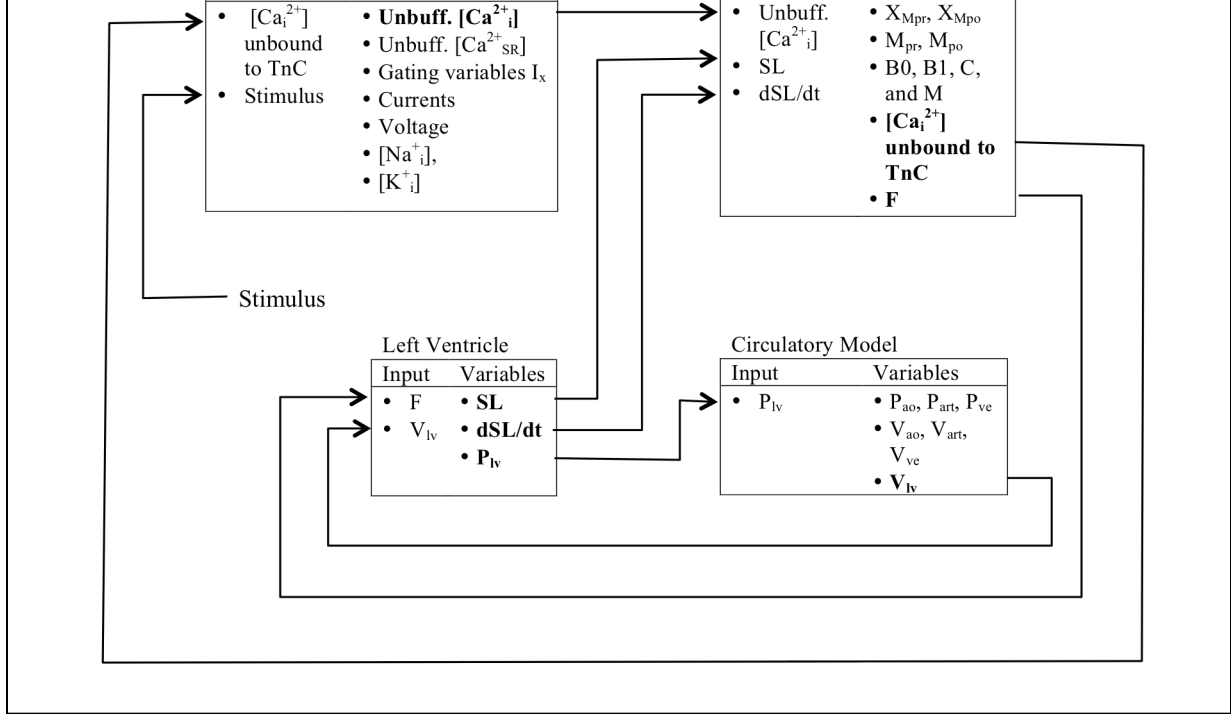
Compartmental Pressure:

$$\frac{dP_i}{dt} = \frac{Q_{in} - Q_{out}}{C_i} \quad (31)$$

2.5 *Model Integration*

We linked together the four sub-models (the electrophysiology of the myocyte, the myofilament system, the left ventricle, and the circulatory system) in order to create a nearly closed-loop system (Fig. 3). The only open loop component of the multi-scale model being the pacemaker stimulus, whose frequency, duration, and amplitude are set at constant values. This stimulus input to the electrophysiology model is used to calculate the values of the state variables in the electrophysiology model, including the unbuffered intracellular calcium concentration. The unbuffered calcium concentration feeds into the myofilament model. The electrophysiology model and the myofilament model have feedback between rates of change of free intracellular calcium, as the ten-Tusscher model describes calmodin buffering of calcium and the myofilament model describes the binding troponin C and calcium. The myofilament model calculates the force of the sarcomere, which is passed into the left ventricle model to get pressure. Pressure is converted into volume in the circulatory system model and fed back into the left ventricle model. The left ventricle model calculates sarcomere length and rate of change of sarcomere length and feeds those values back into the myofilament model.

Figure 3: Integration of the electrophysiology, myofilament, left ventricle, and circulatory system sub-models. Every variable is updated each time step. Bolded variables represent variables being passed between models.



In order to solve this system of differential equations we used an explicit Runge-Kutta numerical integration scheme, via the moderately stiff one-step solver ode23t available in the MatLab© software package. We used a maximum step size of 1ms, as to not miss the short stimulus which has a 2ms duration. We calculated the steady state values for the variables in the ten-Tusscher model by letting the simulation run for 1000ms in the absence of the stimulus. We derived the steady state values for the myofilament variables by deriving the equilibrium states fractions in the absence of muscle contraction. We computed the steady state values for the circulatory model variables by letting the simulation run for 5 cardiac cycles, allowing the fluid pressures and volumes to equilibrate.

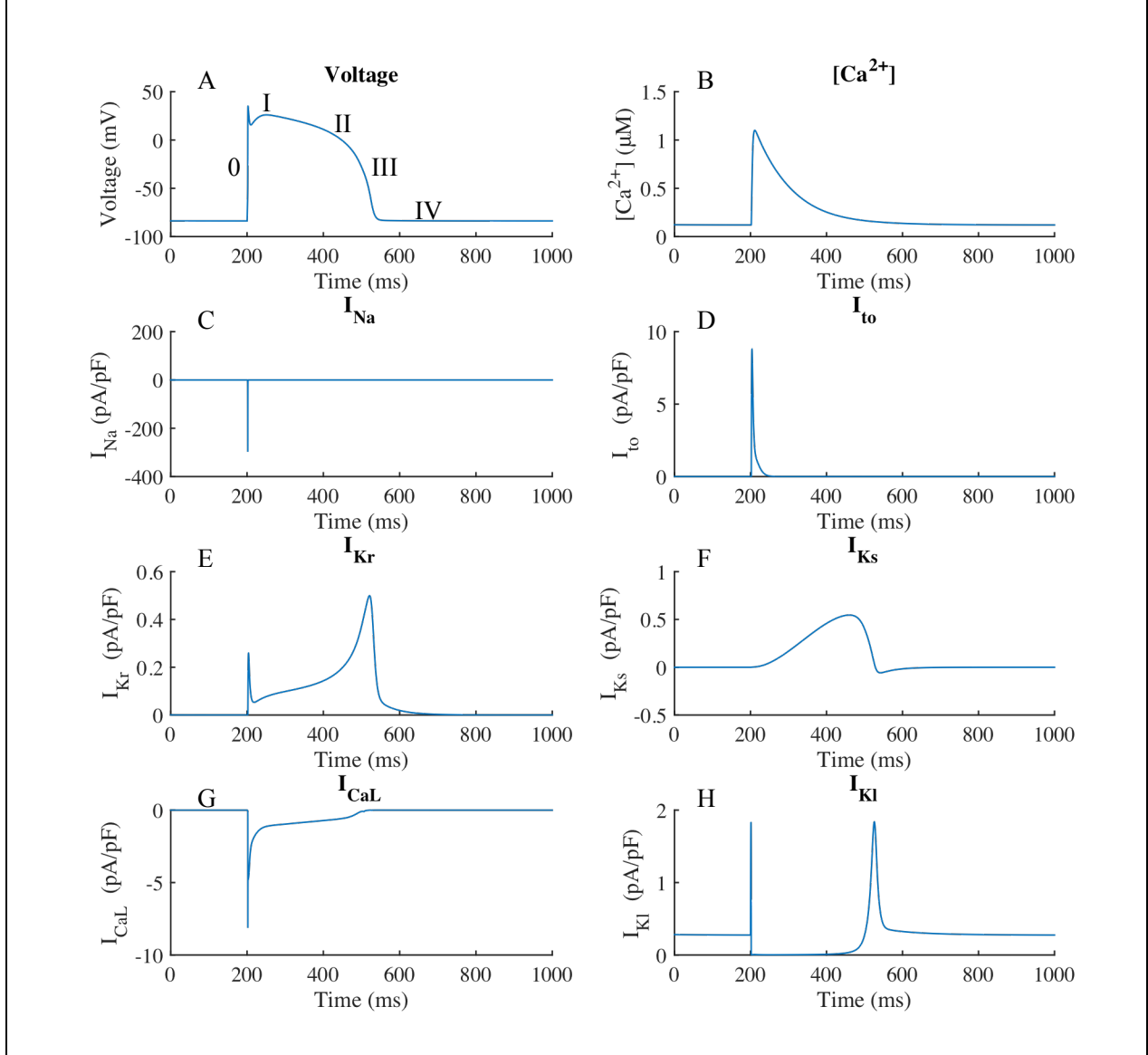
3 Results

3.1 Baseline Data

The model predicts the appropriate shape for the cardiac cycle both on a cellular and a systems level. In Figure 4-A and 4-B, we see the elongated action potential characteristic as well as the spiking and then decaying intracellular calcium transient characteristic of a cardiac cell. Both of these have the shape and order of magnitude as measured data [15].

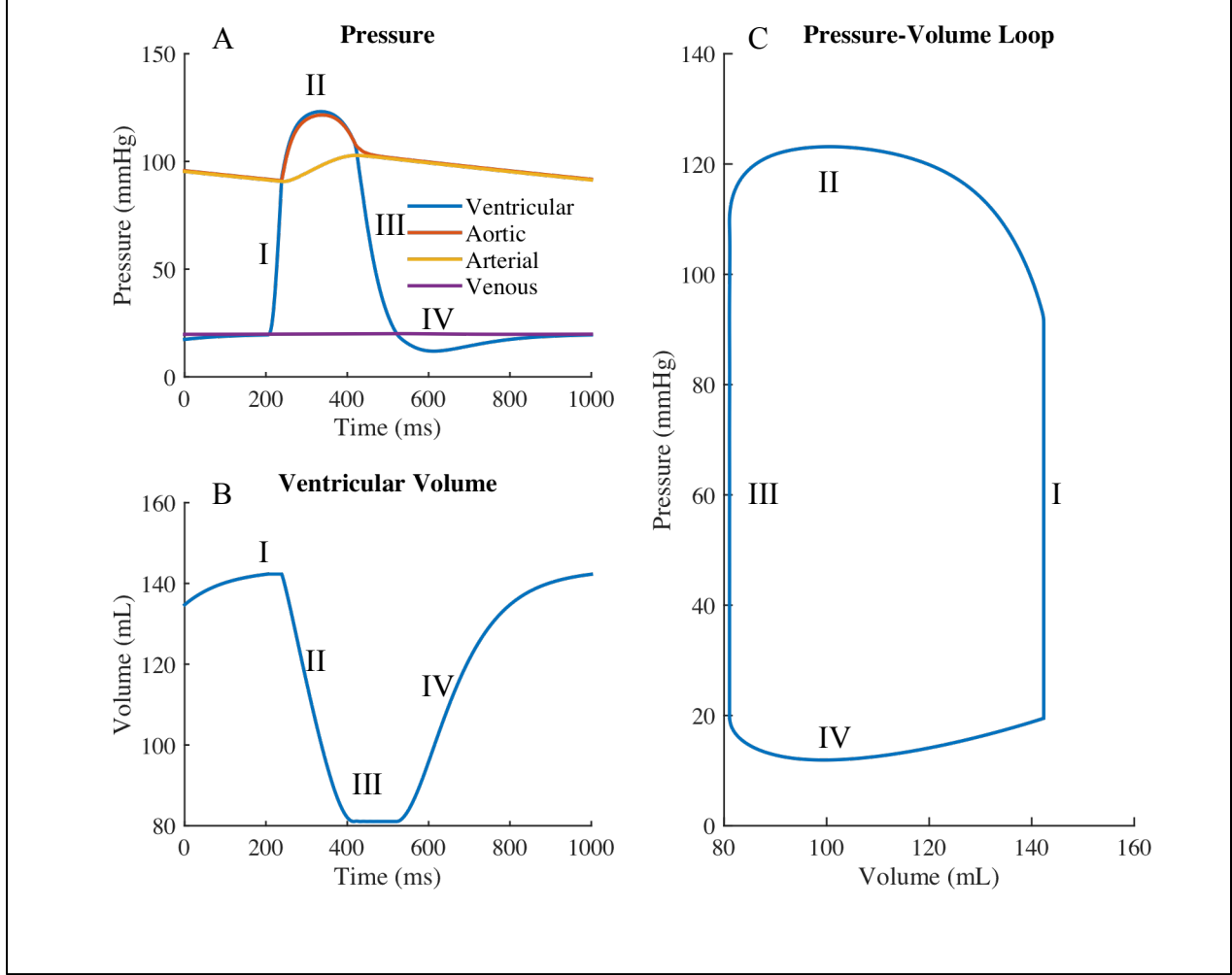
In Figure 4-C through 4-H, we see that our model correctly predicts the ion currents at different times of the action potential. During phase 0, the stimulus causes the opening voltage-gated fast-sodium channel and allows Na^+ to flow into the cell. The influx of positive ions further depolarizes the cell and leads into phase I, during which the fast-sodium channels close and transient outward potassium channels cause outflux of K^+ and a slight repolarization. During phase II, L-type calcium channels open to cause the sarcoplasmic reticulum to release Ca^{2+} ions and the slow delayed rectifier channels cause K^+ to flow out of the cell. During phase III, the L-type calcium channels close and slow delayed inward rectifier current causes K^+ to flow out of the cell, and the inward rectifier current continues through phase IV to fully depolarize the cell so it can cycle through the process again.

Figure 4: Traces of voltage (A), calcium transient (B), fast Na^+ current (C), transient outward K^+ (D), rapid rectifier K^+ (E), slow rectifier K^+ (F), L-type Ca^{2+} (G), and inward rectifying K^+ (H) currents.



The model also correctly predicts the shape of the pressure and volume curves during the cardiac cycle (Fig. 5) and the four stages. In stage I, both valves are closed for isovolumetric contraction. In stage II, the aortic valve opens for ejection. In stage III, the aortic valve closes for isovolumetric relaxation. In stage IV the AV valve opens for filling until the cycle returns to stage and the AV valve closes once again.

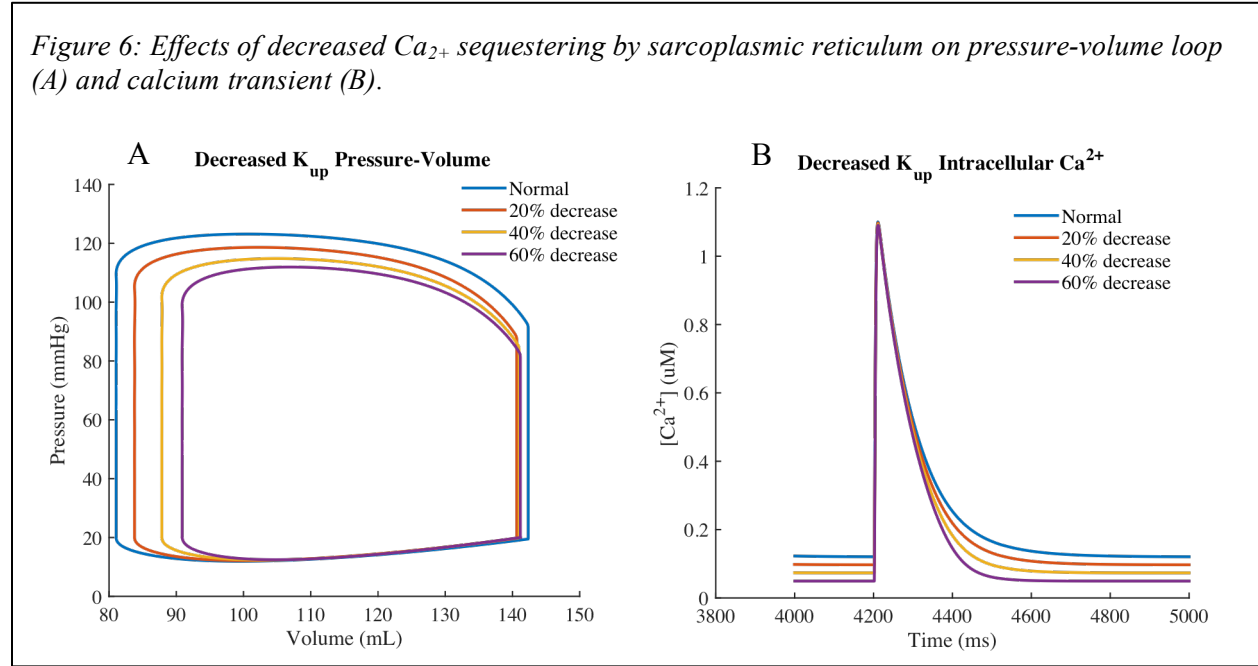
Figure 5: Pressure (A) and volume (B) during the cardiac cycle and the pressure-volume loop (C).



3.2 Calcium Cycling Dysfunction

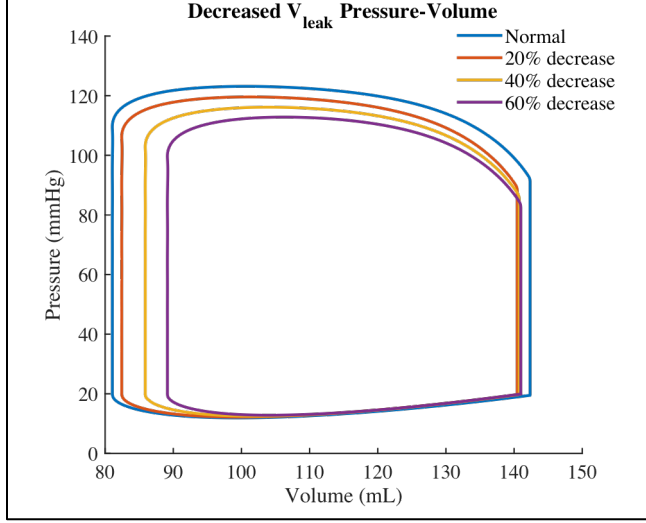
A number of dysfunctions in calcium cycling are associated with heart failure. We investigate the ability of our model to predict and explain the correlations between calcium cycling dysfunction and cardiac performance. First of all, *Olivari et. al. [16]* shows that in patients with human dilated cardiomyopathy calcium sequestering by the sarcoplasmic reticulum is significantly reduced. We model impaired Ca^{2+} uptake by reducing K_{up} in the ten Tusscher model. Our model successfully predicts reduced cardiac output (Fig 6-A). We can see from Fig 6-B that reduced K_{up} decreases Ca^{2+} in the ejection period. This is non-intuitive, but is probably

due to K_{up} shifting the calcium equilibrium closer to buffered intracellular calcium state, preventing the sarcoplasmic reticulum to have enough Ca^{2+} stores to release during contraction and ejection, hence lowering cardiac output.



The literature shows that a number of other variables governing calcium cycling also correlate with heart failure. For example, studies ([17], [18], and [19]) showed that people with heart failure had slightly decreased L-type Ca^{2+} channel density, decreased Na^{+} - Ca^{2+} exchanger activity, and increased fast Na^{+} gate activity. However, our model shows that altering many of the parameters controlling these ion gates have little or no effect on cardiac performance. This may be due to the fact that these parameters, while correlated with heart failure, are not actually causal factors. In patients with these defects an underlying force may be causing both heart failure as well as a change in these parameters.

Figure 7: Effects of increasing Ca_{2+} on pressure-volume loop

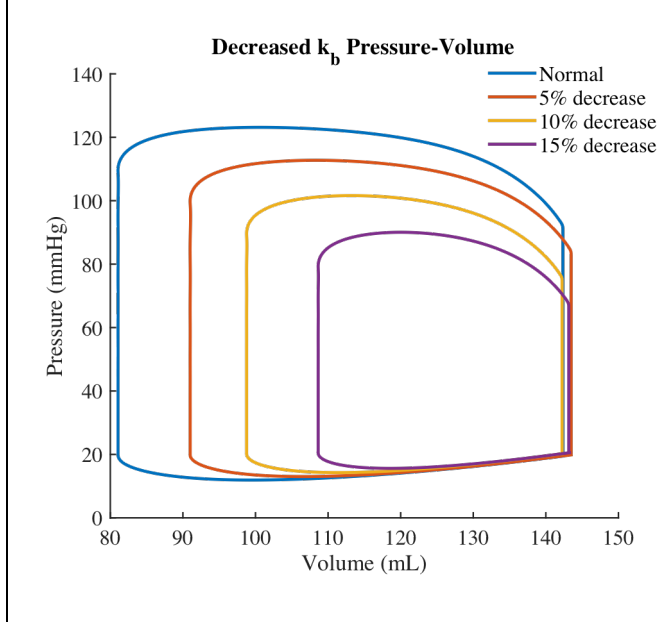


Furthermore, one study [20] showed that an increase in leakage current correlates with cardiac heart failure. Our model actually found the opposite to hold true. In our model, a lower leakage current decreased the total amount of calcium in the system, decreasing contractility and cardiac output (Fig 7). This may mean that the increases in V_{leak} found in the study may

actually be a compensatory effect rather than a causal effect of heart failure, trying to combat other malfunctions, which are actually causing heart failure.

3.3 Cross-bridge Dysfunction

Figure 8: Effect of decreased cross-bridge binding on pressure-volume loop

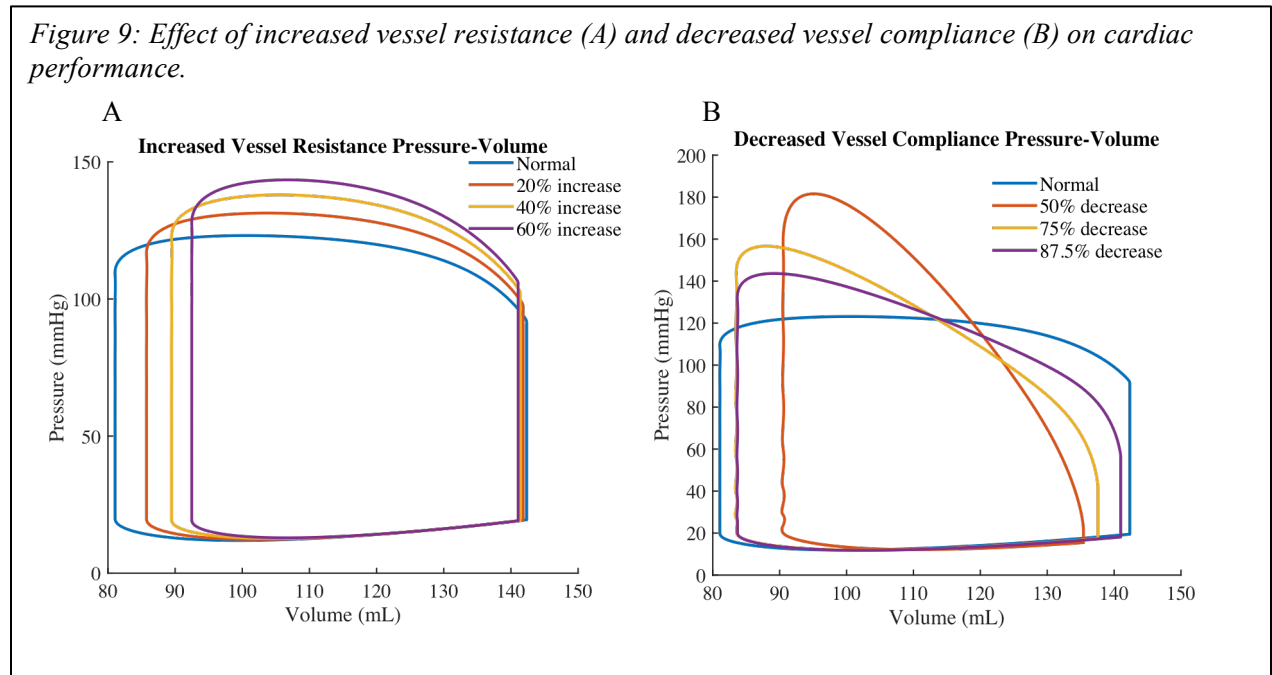


We showed the effect of changing the parameters governing the state transitions rates in the myofilament system. As expected, our model showed decreasing the rates pushing the tropomyosin-actin complex to the myosin-bound state (k_b , h_b , k_{on} in [7]) and increasing the rates pushing the complex away from the myosin-bound state (k_u , h_f , g_{xb} in [7]) decrease contractility and result in heart failure.

Fig. 8 shows the pressure-volume loop for decreased k_b . Decreased h_b and k_{on} and increased k_u , h_f , and g_{xb} showed similar effects.

3.4 Blood Vessel Parameters

We also show that our model can predict changes in cardiac performance with changes in large-scale parameters such as vessel geometry. In Fig. 9-A, we see that increasing afterload resistance (resistance of the vessels) lowers cardiac output and raises systolic pressure, as described in experiments [21]. In Fig. 9-B, we see that decreasing vessel compliance also reduces cardiac output, as well as dramatically reduces length of the contraction phase in the cardiac cycle. A study [22] found the same effects in studying the effects of decreased arterial compliance on heart failure.



4 Discussion

Our model is able to accurately predict cardiac performance on a number of different scales. We can see that the model predicts that changes certain ion gate-related parameters, cross-bridge kinetics, and vessel vasculature all can cause heart failure as is observed in the literature. However, as discussed previously, a number of predictions made by our model disagree with observations in the literature. This may be because these factors are correlated with heart failure, rather than causal. It may also be due to inaccuracies and lack of sophistication in the model. However, the ten-Tusscher is a relatively sophisticated model when it comes to ion gate kinetics, so this is an unlikely explanation with regards to ion-gating variables. However, any discrepancies in blood flow are likely caused by lack of sophistication in our circulatory model, which was a very simple model and does not encompass blood inertia, variable compliance of blood vessels, the right ventricle nor pulmonary circulation- though these would be relatively easy to implement if called for.

In running simulations, we found our model to be surprisingly unstable, particularly in the myofilament model settings. Many combinations rendered the system of differential equations unsolvable or for the limit of some variables to go to infinity. On the opposite end of the spectrum, changing other parameters led to no difference in the cardiac cycle. This raises questions about the intrinsic stability of the cardiac system. By these observations, the cardiac cycle is able to regulate many things through self-feedback with no help from upper neural centers. However, the cardiac system as depicted by this model is unable to compensate for small changes in certain other parameters. These must be controlled by other regulatory mechanisms within the body, such as the baroreceptor response, which controls heart rate and blood vessel vasculature.

In order to enhance the model, we can add a number of things. First of all, adding in the baroreceptor response would not only fix the instabilities associated with the model, but would also create a closed loop system. However, many computational models for the baroreceptor response use time averages of sinoatrial pressure in order to update the baroreceptor response [23], making for a much more difficult integration system. Overall, the model is also very slow, about ten-fold a real time rate. This could be improved by using different integration schemes for the different scales of systems, since something like the action potential needs a much smaller time step of integration than something like blood flow.

5 References

- [1] A Hoes A Mosterd, "Clinical epidemiology of heart failure," *Heart*, vol. 93, no. 9, p. 1137-1146, 2007.
- [2] T Horwich, G Fonarow A Bui, "Epidemiology and risk profile of heart failure," *Nat Rev Cardiol*, vol. 8, no. 1, pp. 30-41, 2011.
- [3] D Ruh, K Foerster, C Heilmann, F Beyersdorf, A Barker, B Jung, A Seifert, F Goldschmidtboeing, P Woias J Ruhhammer, "Arterial strain measurement by implantable capacitive sensor without vessel constriction," *Eng Med Bio Soc*, pp. 535-538, 2012.
- [4] J Boineau, D Saniston T Daniel, "Comparison of Human Ventricular Activation with a Canine Model in Chronic Myocardial Infarction," *Circ*, vol. 44, pp. 74-89, 1971.
- [5] A Huxley A Hodgkin, "A quantitative description of membrane current and its application to conduction and excitation in nerve," *J Phys*, vol. 117, no. 4, pp. 500-544, 1952.
- [6] S Cortassa, B O'Rourke, Y Hashambhoy, J Rice, J Greenstein R Winslow, "Integrative modeling of the cardiac ventricular myocyte," *Wiley Interdiscip Rev Syst. Bio Med*, vol. 3, no. 4, pp. 392-413, 2011.
- [7] F Lionetti, K Campbell, A McCulloch S Campbell, "Coupling of adjacent tropomyosins enhances cross-bridge-mediated cooperative activation in a markov model of the cardiac thin filament," *Biophys J*, vol. 98, no. 10, pp. 224-64, 2010.
- [8] T Karaja, M Guerrisi I Kokalari, "Review on lumped parameter method for modeling blood flow in systemic arteries," *J Biomed Science and Eng*, vol. 6, no. 92-99, 2013.
- [9] W Little H Fukuta, "The Cardiac Cycle and the Physiological Basis of Left Ventricular Contraction, Ejection, Relaxation, and Filling," *Heart Fail Clin*, vol. 4, no. 1, pp. 1-11, 2008.
- [10] D Noble, P Joble, A Paniflov K ten Tusscher, "A model for human ventricular tissue," *Am J Physiol Heart Circ Physiol*, vol. 286, no. 4, pp. 1573-1589, 2004.
- [11] D Beuckelmann L Priebe, "Simulation Study of Cellular Electric Properties in Heart Failure," *Circulation Research*, vol. 82, no. 11, pp. 1206-1223, 1998.
- [12] R Mazhari, R Winslow V Iyer, "A computational model of the human left-ventricular epicardial myocyte,"

- Biophys J*, vol. 87, no. 3, pp. 1507-1525, 2004.
- [13] M Feneley, S Gall, G Maier, J Kisslo, J Davis, J Ranklin, D Glower J Gaynor, "Measurement of left ventricular volume in normal and volume-overloaded canine hearts.," *Am J Phys*, vol. 266, no. 1, pp. 329-340, 1994.
- [14] C Youn, T Heldt, R Kamm, R Mark E Shim, "Computational modeling of the cardiovascular system after Fontan procedure," *Lec Notes in Comp Sci*, vol. 2526, pp. 105-114, 2002.
- [15] P Sutton, M Boyett, M LAb, H Swanton P Taggart, "Human Ventricular Action Potential Duration During Short and Long Cycles," *Circ*, vol. 94, pp. 2526-2534, 1996.
- [16] M Olivari, I Goldenberg, T Levine, D Benditt, A Simon C Limas, "Calcium uptake by cardiac sarcoplasmic reticulum in human dilated cardiomyopathy," *Cardiovasc Res*, vol. 21, no. 8, pp. 601-605, 1987.
- [17] T Kashihara, T Nakada, N Kurebayashi, H Shimojo T Shibazaki, X Sheng, S Yano, M Hirose, M Hongo et al M Horiuchi-Hirose, "Decrease in the density of t-tubular l-type Ca^{2+} channel currents in failing ventricular myocytes," *Am J Physiol Heart Circ Physio*, vol. 300, no. 3, pp. 978-988, 2011.
- [18] R Schwinger, F Schiffer, K Fran, M Sudkamp, F Kuhn-Regnier, G Arnold, M Bohm M Flesch, "Evidence for functional relevance of an enhanced expression of the Na^{+} - Ca^{2+} exchanger in failing human myocardium," *Circulation*, vol. 94, no. 5, pp. 992-1002, 1996.
- [19] L Maier, V Piacentino, J Weisser, G Hasenfuss, R Houser B Pieske, "Rate dependence of $[Na^{+}]_i$ and contractility in nonfailing and failing human myocardium.," *Circulation*, vol. 106, no. 4, pp. 447-453, 2002.
- [20] X Du, "Impaired cardiac contractility response to hemodynamic stress in $\alpha 1$ -deficient mice," *Mol Cell Biol*, vol. 22, no. 8, pp. 2821-2829, 2002.
- [21] J Vincent, "Understanding Cardiac Output," *Cirt Care*, vol. 12, no. 4, p. 174, 2008.
- [22] S Rispler, M Habib, H Sholy, H Hammerman, N aile, D Aronson R Dragu, "Pulmonary arterial capacitance in patients with heart failure and reactive pulmonary hypertension.," *EUr J Heart Fail*, vol. 17, no. 1, pp. 74-80, 2014.
- [23] H Nudelman R Srinivasan, "Modeling the Carotid Sinus Baroreceptor," *Biophys J*, vol. 12, no. 9, pp. 1171-1182, 1972.